CrystEngComm

PAPER

View Article Online
View Journal | View Issue

Cite this: *CrystEngComm*, 2014, **16**, 1525

Li-doped ZnO nanorods with single-crystal quality – non-classical crystallization and self-assembly into mesoporous materials

Carlos Lizandara-Pueyo,[a] Stefan Dilger,[a] Markus R. Wagner,[bc] Melanie Gerigk,[a] Axel Hoffmann[b] and Sebastian Polarz*[a]

Received 22nd August 2013,
Accepted 21st October 2013

DOI: 10.1039/c3ce41670d

www.rsc.org/crystengcomm

The benefits and promise of nanoscale dimensions for the properties of (ceramic) semiconductors are widely known. 1-D nanostructures in particular have proven to be of extraordinary relevance due to their applicability in future electronic and optoelectronic devices. Key to successful technological implementation of semiconductor nanostructures is the control of their electronic properties *via* doping. Despite its tremendous importance, precise chemical doping of defined nano-objects has been addressed rarely so far. Frequent problems are the creation of secondary defects and related undesired property changes by incorporation of hetero-elements, and the difficulty in ensuring a uniform and precise positioning of the dopant in the nanocrystal lattice. Here, we present the synthesis of Li-doped zinc oxide nanorods, which possess excellent (single-crystal) quality. The method is based on a novel non-classical crystallization mechanism, comprising an unusually oriented disassembly step. Afterwards, the nanorods are incorporated into mesoporous layers using colloidal self-assembly. Proof-of-principle gas sensing measurements with these novel materials demonstrate the beneficial role of Li-doping, indicating not only better conductivity but also the occurrence of catalytic effects.

1. Introduction

The exploitation of semiconductors is of utmost importance to existing and forthcoming technologies. Some have even argued that in analogy to the 'Copper Age' following the 'Stone Age', we are currently living in the Semiconductor Age.[1] For sure, silicon is the semiconductor which is used the most in a technological context (*e.g.* microelectronics). However, there are various applications for which silicon is not suitable due to either its relatively narrow band-gap or its indirect band-structure. Therefore, there is large interest in wide, direct gap semiconductors like III/V compounds, for instance gallium nitride (GaN),[2–4] or II/VI compounds such as zinc oxide (ZnO).[5–7] Furthermore, for silicon, it is well documented that the pure compound itself is only of very limited use. Functional devices like photovoltaic cells require p- and n-doped Si. Interestingly, the exploitation of doping to control the properties of ceramic semiconductor nanostructures still stands at the beginning.[8–11] Most nanomaterials presented in the literature consist of the pure semiconductor, or unintentional doping with impurities has occurred.

Zinc oxide, one of the most important binary semiconductors in current research,[12,13] is interesting because of its multifunctional character with applications in various fields such as optoelectronics (*e.g.* photovoltaics, transparent electronics),[14] cosmetics (UV protection), sensor technology (gas sensors, bio sensors) or catalysis (methanol synthesis).[6,15–17] One-dimensional ZnO nanostructures have also attracted significant attention.[14] Despite much recent research, important challenges remain.[18] ZnO is intrinsically n-doped due to its tendency to form native point defects and due to the presence of residual shallow donors such as interstitial hydrogen or of Al, Ga, or In on Zn lattice sites.[19–21] Major efforts have been undertaken to achieve p-doping of ZnO *via* partial substitution of zinc by lithium or,[10,11] alternatively, of oxygen by nitrogen.[22–24] The desired p-doping has often been found to be compensated by unintentional n-doping resulting from dopants being located on interstitial sites in the lattice.[25,26] The development of reliable methods for the preparation of Li–ZnO colloidal particles, ultimately of nanorods, with precise lattice site control of the dopants, would thus represent a major advance.

Particular importance in this context is attributed to routes leading to colloidal ZnO nanorods. A common way to prepare ZnO is to start from an aqueous solution of a Zn^{2+} salt (*e.g.* zinc acetate), followed by the precipitation of zinc–oxo–hydroxo

[a] *University of Konstanz, Universitaetsstr. 10, 78464 Konstanz, Germany. E-mail: sebastian.polarz@uni-konstanz.de; Fax: +49 7531 884406; Tel: +49 7531 884415*
[b] *Technical University of Berlin, Hardenbergstr. 36, 10623 Berlin, Germany*
[c] *Catalan Institute of Nanotechnology (ICN), Campus UAB, 08193 Bellaterra (Barcelona), Spain*

species at elevated pH and elimination of water resulting in ZnO.[27,28] Guo and Xu *et al.* and independently Weller *et al.* prepared single-crystalline ZnO nanorods in 2002.[29,30] Water is a highly polar, protic solvent, and it permits Ostwald-ripening as an equilibrating process due to the sufficient solubility of the ions Zn^{2+} and OH^- in the continuous phase. Therefore, it is tempting to prepare ZnO nanostructures in organic, non-coordinating solvents. There are only a few reports about the preparation of ZnO in aprotic, organic solvents, which is mainly due to the lack of precursors which are soluble enough in these media. Chaudret *et al.* have published a series of highly interesting papers about the reaction of dialkylzinc compounds to zinc oxide colloids in cyclohexane.[31–36] For instance, the authors described the successful synthesis of defined nanorods and nanodiscs.[31]

Experimental section

The zinc oxide precursor was prepared as described in previous papers.[37–39] All other chemicals were obtained from chemical suppliers and were purified and/or dried prior to use.

Preparation of nanorods

Water (1.5 ml), cyclohexane (35 ml) and a polyglyceryl-containing emulsifier like polyglyceryl-3 polyricinoleate (1 ml) are mixed. For the synthesis of Li-containing materials, Li-salts (lithium acetate, lithium stearate) are added to the aqueous phase. An emulsion is prepared by applying ultrasound for 15 min using a Bandelin-Sonopuls TT13/FZ ultrasonication device. The emulsion is heated to 70 °C. $[MeZnOiPr]_4$ is dissolved in dry cyclohexane (15 ml) and added drop-wise at 0.63 ml min^{-1} to the emulsion using a syringe pump from KD Scientific (model KS200). During the addition, ultrasonication is continued for 300 min. The final colloids are isolated by removing the solvent under vacuum.

Characterization methods

PXRD data were acquired using a Bruker D8 Advance. Conventional TEM measurements were performed using a Zeiss Libra 120, while high resolution TEM measurements were performed using a Jeol JEM2200FS. Solid-state NMR spectra were recorded using a Bruker DRX 400 spectrometer. N_2 physisorption measurements were recorded using a Micromeritics TriStar. The Raman spectra were recorded using a LabRAM HR800 spectrometer (HORIBA Jobin Yvon) with the 532 nm laser line of a frequency doubled Nd:YAG laser. The laser was focused on the sample using an Olympus MplanN 100× objective lens (NA = 0.90). The spectra were collected in backscattering geometry with a spectral resolution better than 0.3 cm^{-1}. The spectrally dispersed Raman signal was detected using a Peltier-cooled CCD camera. The laser power on the sample was tuned to 1 mW. Micro-photoluminescence (μPL) spectra were measured using the fourth harmonic (266 nm) of a pulsed Nd:YAG laser (Coherent Antares 76s) with a repetition rate of 76 MHz and a pulse length of 50 ps as excitation source. The laser was focused through a UV enhanced objective lens (NA = 0.65) on the samples which were mounted on a helium flow cryostat and cooled to a temperature of T = 4 K. The excitation power was kept below 100 μW to avoid local heating or high excitation effects. The luminescence was spectrally dispersed and recorded using a 1 m spectrometer (SPEX) with a UV enhanced CCD (Princeton Instruments) achieving a spectral resolution of 0.01 nm. Time resolved photoluminescence (TRPL) measurements were performed by single photon counting using a micro channel plate with a bialkali cathode as detector (Hamamatsu R3809 U-52). The emitted light was dispersed using a subtractive double monochromator (McPherson) at a spectral resolution of 0.1 nm. EPR measurements were performed using an X-band Miniscope spectrometer (MS200, Magnettech GmbH).

Gas sensor preparation

8 mg of the colloid samples were dispersed in 4 mL of ethanol (abs.) by ultrasonication. The dispersions were drop coated on 3 mm × 3 mm sensor substrates from "Umweltsensortechnik". Ten drops of the dispersion were subsequently dropped onto the substrate and allowed to dry. The organic, colloidal stabilizers were removed in air at 475 °C during 5 hours. The overall gas stream through the setup was kept constant at 0.5 L min^{-1} (80% N_2, 20% O_2). The ethanol concentration (5×10^3 ppm) was adjusted using an OWL-stone OVG-4 setup. The sensors were heated by varying the heater voltage (10 Ω heating resistor built into the sensor substrate). Temperatures at the sensor were measured with a type K thermocouple, and the electric current through the sensor was measured using a Keithley 2401 source meter at a constant measuring voltage of 2 V.

Results and discussion

Li–ZnO nanorods *via* non-classical crystallization

Based on our experience with the use of alkylzinc alkoxides $[MeZnOR]_4$ (R = organic group) as ZnO precursors, and regarding the preparation of colloidal ZnO nanoparticles with characteristic shape anisotropy,[37,40,41] the following experiment was designed (see also the experimental section): a water-in-oil emulsion is prepared, and $[MeZnOR]_4$ is added to the oil-phase by way of a syringe pump, which allows control of the precursor concentration at all times. The precursor is hydrolyzed in the vicinity of the oil–water interface, and ZnO formation is initiated. Li^+ ions can be introduced by dissolving lithium species in the aqueous phase of the emulsion.

A unique mechanism for the formation of the final particles is revealed by transmission electron microscopy (TEM) images of samples taken from the reaction mixture at different times. At t = 5 min, a great number of spherical particles have formed (Fig. 1). These particles are amorphous, as shown by the absence of any pattern in electron diffraction (ED). Apparently, the water droplets have gelated. One also sees some larger particles composed of several smaller ones (Fig. 1c). After t = 15 min, the TEM data show that the

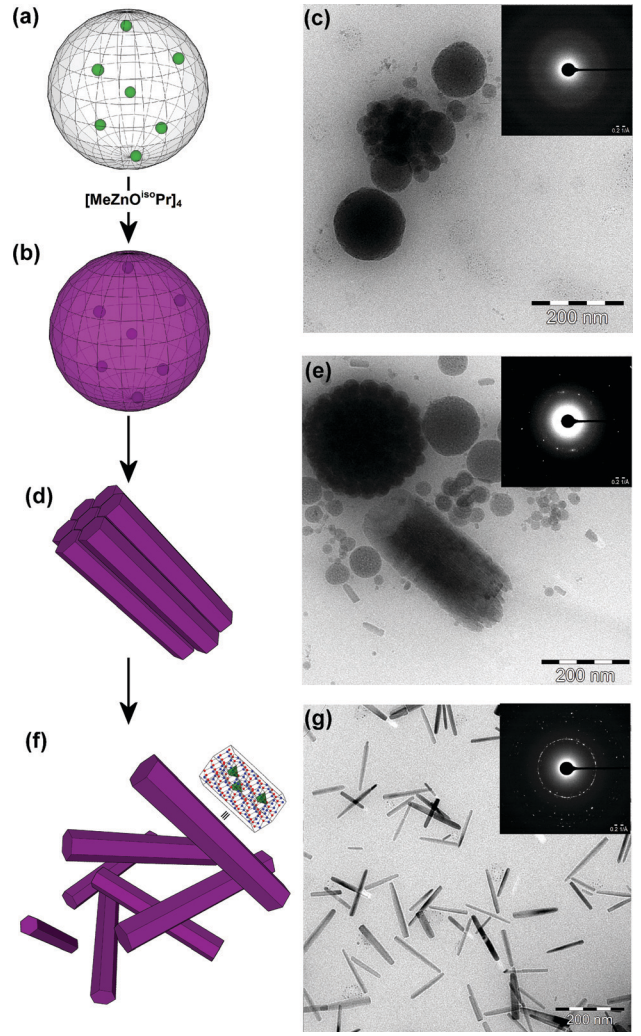

Fig. 1 Schematic representation of the formation mechanism (left side) and time-dependent TEM and ED data (right side). Indication of one water droplet containing lithium ions plotted in green (a); the gelated, spherical particles after addition of the ZnO precursor (b) and the corresponding TEM data recorded after t = 5 min (c); crystallization of a bundle of rod-like nanocrystals (d, e; t = 15 min); detachment of the particles into isolated nanorod colloids (f, g). An excerpt of the ZnO lattice with Li replacing tetrahedral zinc sites is also shown.

intermediary amorphous phase starts to crystallize (Fig. 1e). Surprisingly, the results of this crystallization process are bundles of highly oriented nanorods, a so-called super-crystal.[41] In agreement with this, a large degree of orientation is apparent not only from the TEM images but also from the ED pattern, which is characterized by spots rather than rings. Finally, after t = 100 min, the entire sample consists of crystalline nanorods with lengths of 100–200 nm and widths of ≈15 nm.

The described crystallization mechanism is highly unusual. Unlike classical crystallization, it does not involve nucleation followed by growth *via* attachment of single ions. The process just described is much closer to many systems reported in biomineralization,[42] where complex shapes are generated *via* crystallization of an intermediary and often amorphous phase inside confining compartments like cellular vesicles.

The polydispersity of the size-distribution proved to be changeable by adapting a method known as focusing.[43] Feeding the precursor in a continuous way allowed an adjustment of the aspect ratio. The more and the longer the precursor is added, the longer the particles become (Fig. 2). To find out about the main growth direction, powder X-ray diffraction (PXRD) was recorded and is shown in Fig. 2e.

The observed pattern is characteristic of ZnO in the wurtzite modification. PXRD indicates that the particles are elongated along the *c*-direction. It is apparent that the signal corresponding to elongation of the particles in the *c*-direction, the [002] diffraction at 2θ = 34.4°, is much narrower and becomes more intense as the particles get more elongated. Particle extensions can be obtained *via* the evaluation of the widths of the [100] signal (for the *a*,*b* direction) and the [002] signal (for the *c*-direction) using the Scherrer equation.[44,45] It can be concluded that the extension of the growth phase affects mainly the crystallographic *c*-direction D_c = 55 → 120 nm, while $D_{a,b}$ = 15 nm remains almost constant.

The non-classical crystallization pathway is the key to the successful incorporation of Li so as to replace Zn in the ZnO lattice, because Li ions dissolved in the water droplet of the emulsion become entrapped during the solidification (Fig. 1b,d,f). The characterization of the Li-containing material is a demanding task. This is because Li, as a very light element, cannot be detected using energy-dispersive X-ray spectroscopy (EDX). Furthermore, the ionic radius of Li^+ in tetrahedral coordination (59 pm) is so close to the radius of Zn^{2+} in wurtzite (60 pm) that a differentiation using

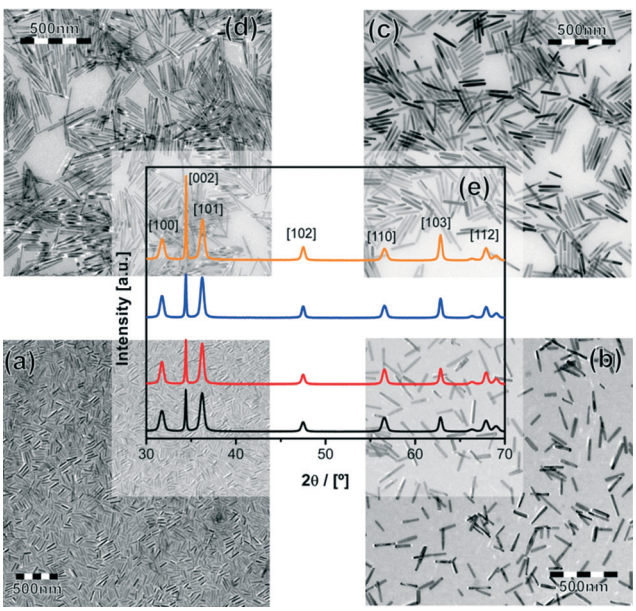

Fig. 2 TEM (a–d) and PXRD data (e) of samples prepared for continuous addition of ZnO precursor (a; black graph ↔ a; red graph ↔ b; blue graph ↔ c; orange graph ↔ d).

crystallographic methods is not possible either. Therefore, the formation of the desired $Zn_{1-x}Li_xO$ materials (LZO) was investigated using a combination of more sophisticated, independent analytical methods (Fig. 3). The composition, $x = 0.103$, was determined from elemental analysis using ion-coupled plasma mass spectrometry (ICP-MS) together with NMR-data. ^{7}Li solid-state NMR spectroscopy, a sensitive tool for investigating the local environment of the lithium ions, shows two species at δ = 1.83 and 1.04 ppm. The latter species originates from residual, non-incorporated Li-salt as shown by reference measurements (Fig. 3a). The residual Li^+ could be separated by purifying the samples using a Li-specific crown ether (12-crown-4).

It can be seen that only one signal remains, which is characteristic of Li^+ on Zn^{2+} lattice sites (Fig. 3a). Vibrational modes and strain in the Li-doped nanorods were studied using micro Raman spectroscopy and compared to a pure ZnO nanorod sample with an identical aspect ratio as reference (Fig. 3b). Both samples show the typical ZnO lattice modes with narrow line widths of only 1.5 cm^{-1} in case of the E_2(low), which is comparable to excellent ZnO single crystals.[46] No broadening of modes is observed in the Li-doped samples. This indicates that the structural quality of the nanorods is not reduced by the Li^+ incorporation. The strain-sensitive E_2(high), observed at 439.4 cm^{-1} in both samples, is characteristic of a small compressive strain.[47,48] The identical position of this mode in the Li doped and undoped nanorods proves that no additional lattice strain is induced by the Li doping. In addition to the ZnO modes, the Li doped samples show Raman modes at 95.6, 127.2, 156.8, 193.6, 271.4 and 1091.0 cm^{-1} with exceptional intensities. These modes appear exclusively in Li doped ZnO and thus provide clear evidence for the incorporation of Li into the ZnO nanorods.[48,49]

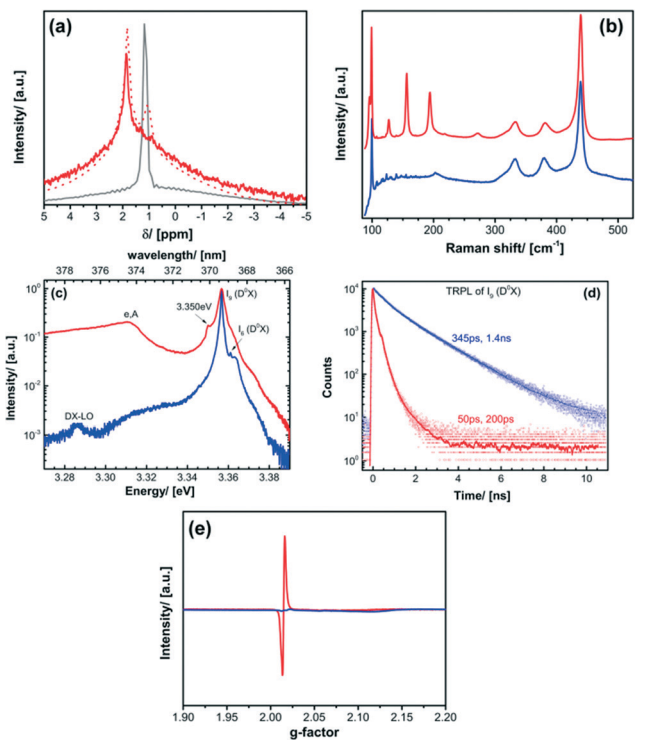

Fig. 3 Spectroscopic investigation of LZO nanorods (≡red) in comparison to ZO nanorods (≡blue): (a) ^{7}Li solid-state NMR spectra of LZO rods (prior ≅ dotted line, after purification ≅ solid line) and lithium stearate (≡grey line) as reference. (b) Raman spectra taken at room temperature. (c) PL spectra taken at T = 5 K. Both spectra are normalized to neutral donor bound exciton luminescence at 3.3567 eV (I_9). (d) TRPL of I_9 (D^{0}X). (e) X-band EPR spectra.

In addition, optical emission spectra were recorded (Fig. 3c). The low temperature photoluminescence (PL) spectrum is dominated by a bound exciton luminescence (DX) at 3.3567 eV which coincides with the reported peak position of the I_9 line in ZnO.[19] In the emission spectra of the LZO nanorods, an additional emission band with a maximum at 3.31 eV is observed, which corresponds to a free electron to acceptor transition (e,A).[50] Recombination dynamics of the DX transitions, studied by time-resolved photoluminescence (TRPL) measurements in both samples, show moreover that an exciton lifetime of 1.4 ns in the undoped sample is exceptionally long – *i.e.* comparable to that of high quality ZnO single crystals and shortens to 0.2 ns in the LZO nanorods, possibly due to non-radiative energy transfer to deeper Li-related electronic states.[51] Furthermore, a new signal at a g-factor of 2.014 appears in electron paramagnetic resonance (EPR) spectroscopy measurements of LZO. This signal is characteristic of heteroatoms occupying Zn^{2+} lattice sites.[25,52,53]

All of the mentioned analytical data lead to the conclusion that the nanorods prepared by our method possess excellent single-crystal-like quality. The high crystallinity could be confirmed by HRTEM measurements shown in Fig. 4a, b. ED diffraction (not shown) confirms that the long axis of the single-crystalline nanoparticles is equal to the crystallographic c-direction. The value of the lattice constant $c = 2 \times d_{002}$ is 5.18 (±0.013) Å, which is the same value as that of single-crystalline ZnO. There is practically no difference from nanorods consisting of pure ZnO (Fig. 4c).

Assembly of novel, mesoporous materials

LZO nanorods represent promising nanoparticle building blocks for advanced functional devices. Here, we introduce a unique method in which the formation of such devices is driven mainly by self-organization. From TEM images shown in Fig. 2, it is apparent that the nanorods tend to align parallel to each other at high concentrations. Drying of a dispersion with higher concentrations of the nanorods leads to the formation of mesoscopic structures, which have been investigated using scanning electron microscopy (SEM) as shown in Fig. 5b. The removal of organic compounds located at the ZnO interfaces for stabilization *via* calcination leads to a novel porous material and at the same time to a network of electrically connected nanorods (see Fig. 5c, d). The porous nature and the reminiscent orientation of the nanorods are clearly apparent from TEM. Formation of a mesoporous material with an average pore size of 8.5 nm is proven by its N_2 physisorption isotherm and pore-size distribution function, as shown in

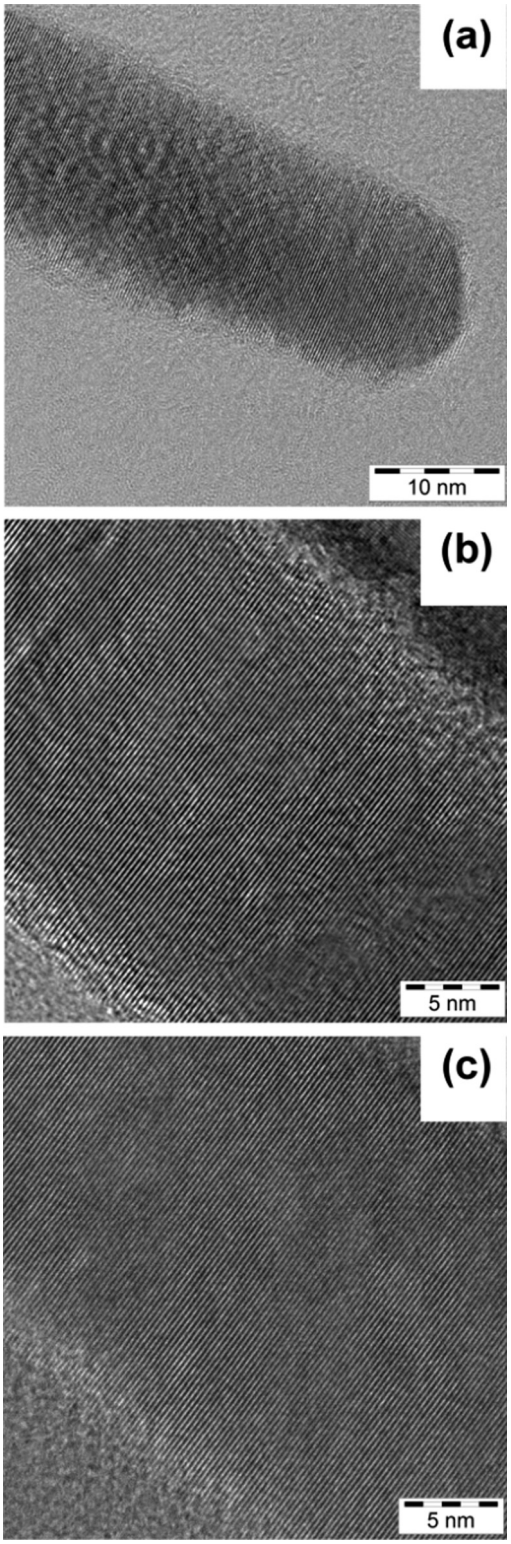

Fig. 4 HRTEM micrographs of Li-containing ZnO nanorods (a, b) in comparison to pure ZnO nanorods (c).

Fig. 5c. To the best of our knowledge, this is the first time that formation of a porous material of this kind has been achieved.

In order to demonstrate the benefits of this special material's architecture with regard to its functionality, *e.g.* for chemical gas-sensing,[54] the porous solid described above is brought between an interdigitating array of electrodes (Fig. 5d). Working at constant voltage and constant reactant concentration, the current was measured as a function of the temperature at the sensor. Direct comparison of LZO to an analogous material composed of pure ZnO (Fig. 6a) shows that the current for LZO is always higher than that for ZnO, a direct consequence of

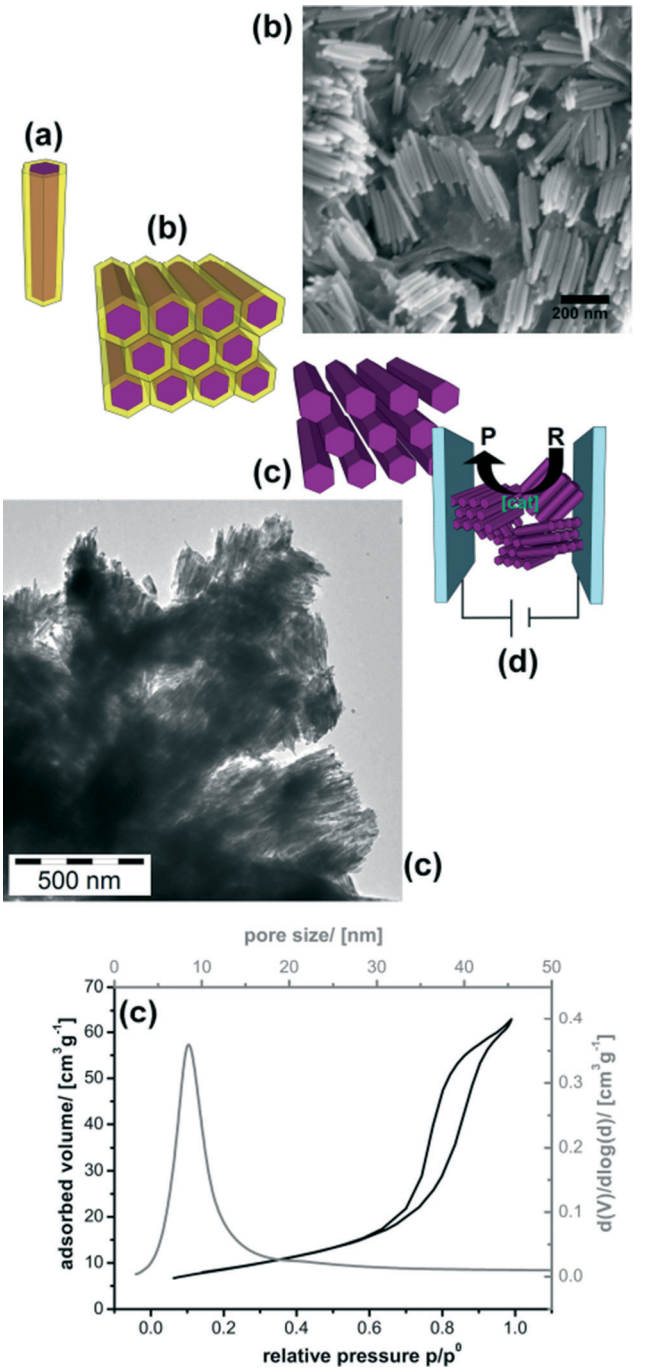

Fig. 5 Oriented attachment (b; SEM data and schematic image) of single LZO nanorods (a). The porous nanorod material obtained after calcination (c; TEM data, nitrogen physisorption data and pore-size distribution function and schematic image). Device architecture for testing the materials in chemical sensing (d).

the lower resistance due to the successful doping described above.

A direct advantage of the higher overall conductivity is that the sensor device affords reliable results at comparably low temperatures. As the usual temperature for the operation of conventional gas sensors is 300–400 °C, data of very poor quality are obtained with pure zinc oxide material at a much lower temperature of 150 °C. Even at this low temperature however, the LZO sensor produces a clear signal as soon as the reactant gas is turned on. However, also the response of the sensor is of importance (respectively the measured currents prior to and after exposure to the analyte).

The current is a direct measure of the conversion of the reactant (R ≅ ethanol) into the products (P ≅ carbon dioxide, water)[55] at the surfaces. Thus, the temperature dependency of the current amplification (Fig. 6b) can be evaluated using the Arrhenius formalism. Indeed, there is a difference in current amplification. It can be seen that the LZO material is superior to the materials prepared in an analogous way, except for nanorods composed of pure ZnO. Fitting the data to the Arrhenius law affords virtual activation energies for the surface processes

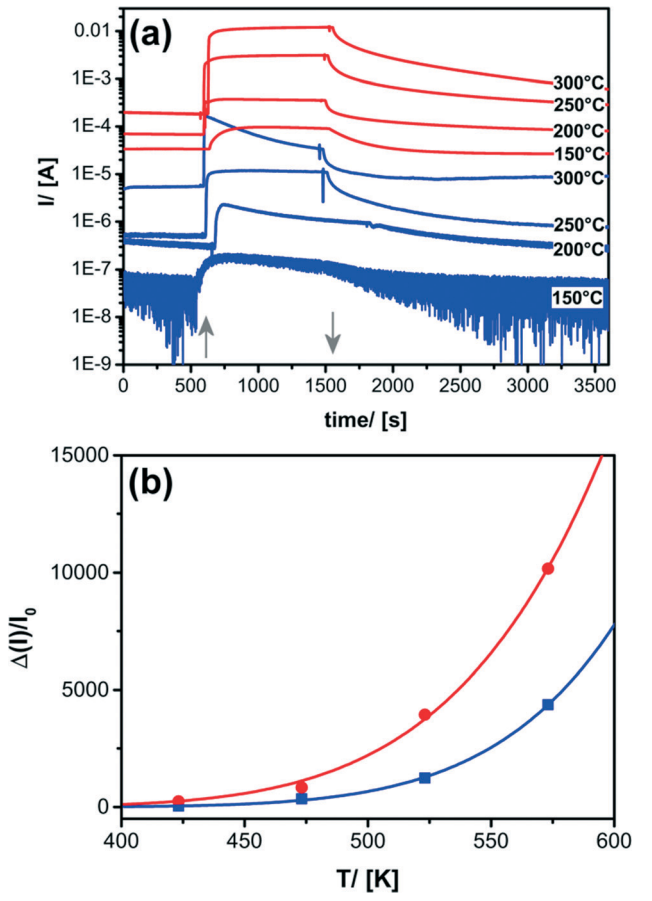

Fig. 6 (a) Results of the gas sensing experiments for the mesoporous LZO material (red graphs) compared to an analogous, mesoporous material composed of pure ZnO nanorods (blue graphs) as a reference. The grey arrow indicates when the ethanol gas is switched on and off. (b) Current amplification factor as a function of temperature (data points) and exponential fit curves according to the Arrhenius law.

($E_{a,LZO}$ = 49.8 kJ mol^{-1}, $E_{a,ZO}$ = 61.31 kJ mol^{-1}). The lowering of activation energy is indicative of a catalytic effect caused by Li-incorporation. The latter assumption is supported by the difference in temporal behavior of the two materials. Whereas the sensing signal of pure ZnO decreases more or less slowly for continuing exposure to the analyte, LZO is characterized by a constant or even increasing sensor response.

Conclusions

Our results open new vistas toward a controlled doping of nanoparticles, and in particular of those with anisotropic shape, by use of a non-classical crystallization methodology related to biomineralization. It could be revealed that anisotropic ZnO particles form from an amorphous precursor state followed by an unusual disassembly step. Li^+ could be incorporated without losing the perfect crystallinity of the rod-like nanoparticles. It was proven by several methods that Li^+ occupies the Zn^{2+} position in the ZnO lattice, resulting in higher electric conductivity than conventional ZnO. The nanorods could be reassembled into a parallel array. This array was converted into a unique mesoporous material, which could be used for the fabrication of functional devices. By facilitating chemical gas-sensing measurements, our results provide a unique perspective with regard to testing the catalytic activities of nanostructured materials.

Acknowledgements

We gratefully acknowledge the Carl-Zeiss Foundation for funding (REFINE research initiative). We thank Prof. A. Seubert (Marburg) for performing the ICP-MS measurements.

Notes and references

1 R. F. Service, *Science*, 2000, **287**, 415–417.
2 S. N. Mohammad and H. Morkoc, *Prog. Quantum Electron.*, 1996, **20**, 361–525.
3 F. A. Ponce and D. P. Bour, *Nature*, 1997, **386**, 351–359.
4 M. Law, J. Goldberger and P. D. Yang, *Annu. Rev. Mater. Res.*, 2004, **34**, 83–122.
5 Z. L. Wang, *Mater. Today*, 2004, **7**, 26–33.
6 Z. L. Wang, *J. Phys.: Condens. Matter*, 2004, **16**, R829–R858.
7 U. Ozgur, Y. I. Alivov, C. Liu, A. Teke, M. A. Reshchikov, S. Dogan, V. Avrutin, S. J. Cho and H. Morkoc, *J. Appl. Phys.*, 2005, **98**, 041301.
8 S. J. Pearton, D. P. Norton, K. Ip, Y. W. Heo and T. Steiner, *Prog. Mater. Sci.*, 2005, **50**, 293–340.
9 C. B. Geller, W. Wolf, S. Picozzi, A. Continenza, R. Asahi, W. Mannstadt, A. J. Freeman and E. Wimmer, *Appl. Phys. Lett.*, 2001, **79**, 368–370.
10 S. C. Erwin, L. Zu, M. I. Haftel, A. L. Efros, T. A. Kennedy and D. J. Norris, *Nature*, 2005, **436**, 91–94.
11 G. Galli, *Nature*, 2005, **436**, 32–33.
12 A. P. Alivisatos, *Science*, 1996, **271**, 933–937.
13 H. Weller, *Adv. Mater.*, 1993, **5**, 88–95.

14 S. Ju, A. Facchetti, Y. Xuan, J. Liu, F. Ishikawa, P. Ye, C. Zhou, T. J. Marks and D. B. Janes, *Nat. Nanotechnol.*, 2007, **2**, 378–384.
15 M. Graetzel, *J. Photochem. Photobiol., C*, 2003, **4**, 145–153.
16 M. Law, L. E. Greene, J. C. Johnson, R. Saykally and P. Yang, *Nat. Mater.*, 2005, **4**, 455–459.
17 Q. Wan, Q. H. Li, Y. J. Chen, T. H. Wang, X. L. He, J. P. Li and C. L. Lin, *Appl. Phys. Lett.*, 2004, **84**, 3654–3656.
18 D. E. Perea, E. R. Hemesath, E. J. Schwalbach, J. L. Lensch-Falk, P. W. Voorhees and L. J. Lauhon, *Nat. Nanotechnol.*, 2009, **4**, 315–319.
19 B. K. Meyer, H. Alves, D. M. Hofmann, W. Kriegseis, D. Forster, F. Bertram, J. Christen, A. Hoffmann, M. Straßburg, M. Dworzak, U. Haboeck and A. V. Rodina, *Phys. Status Solidi B*, 2004, **241**, 231–260.
20 B. K. Meyer, J. Sann, S. Lautenschläger, M. R. Wagner and A. Hoffmann, *Phys. Rev. B: Condens. Matter Mater. Phys.*, 2007, **76**, 184120.
21 M. D. McCluskey and S. J. Jokela, *J. Appl. Phys.*, 2009, **106**, 071101–071113.
22 M. G. Wardle, J. P. Goss and P. R. Briddon, *Phys. Rev. B: Condens. Matter Mater. Phys.*, 2005, **71**, 155205.
23 D. C. Look and B. Claftin, *Phys. Status Solidi B*, 2004, **241**, 624–630.
24 A. Tsukazaki, A. Ohtomo, T. Onuma, M. Ohtani, T. Makino, M. Sumiya, K. Ohtani, S. F. Chichibu, S. Fuke, Y. Segawa, H. Ohno, H. Koinuma and M. Kawasaki, *Nat. Mater.*, 2005, **4**, 42–46.
25 V. Ischenko, S. Polarz, D. Grote, V. Stavarache, K. Fink and M. Driess, *Adv. Funct. Mater.*, 2005, **15**, 1945–1954.
26 B. Claflin, D. C. Look, S. J. Park and G. Cantwell, *J. Cryst. Growth*, 2006, **287**, 16–22.
27 M. Ohyama, H. Kozuka and T. Yoko, *Thin Solid Films*, 1997, **306**, 78–85.
28 L. Guo, S. H. Yang, C. L. Yang, P. Yu, J. N. Wang, W. K. Ge and G. K. L. Wong, *Appl. Phys. Lett.*, 2000, **76**, 2901–2903.
29 L. Guo, Y. L. Ji, H. Xu, P. Simon and Z. Wu, *J. Am. Chem. Soc.*, 2002, **124**, 14864.
30 C. Pacholski, A. Kornowski and H. Weller, *Angew. Chem., Int. Ed.*, 2002, **41**, 1188.
31 M. Monge, M. L. Kahn, A. Maisonnat and B. Chaudret, *Angew. Chem., Int. Ed.*, 2003, **42**, 5321–5324.
32 M. L. Kahn, T. Cardinal, B. Bousquet, M. Monge, V. Jubera and B. Chaudret, *ChemPhysChem*, 2006, **7**, 2392–2397.
33 M. L. Kahn, M. Monge, V. Colliere, F. Senocq, A. Maisonnat and B. Chaudret, *Adv. Funct. Mater.*, 2005, **15**, 458–468.
34 M. L. Kahn, M. Monge, E. Snoeck, A. Maisonnat and B. Chaudret, *Small*, 2005, **1**, 221–224.
35 C. Pages, Y. Coppel, M. L. Kahn, A. Maisonnat and B. Chaudret, *ChemPhysChem*, 2009, **10**, 2334–2344.
36 F. Rataboul, C. Nayral, M. J. Casanove, A. Maisonnat and B. Chaudret, *J. Organomet. Chem.*, 2002, **643**, 307–312.
37 C. Lizandara-Pueyo, S. Siroky, M. R. Wagner, A. Hoffmann, J. S. Reparaz, M. Lehmann and S. Polarz, *Adv. Funct. Mater.*, 2011, **21**, 295–304.
38 S. Dilger, C. Lizandara-Pueyo, M. Krumm and S. Polarz, *Adv. Mater.*, 2012, **24**, 543–548.
39 C. Lizandara-Pueyo, M. W. E. van den Berg, A. De Toni, T. Goes and S. Polarz, *J. Am. Chem. Soc.*, 2008, **130**, 16601–16610.
40 S. Polarz, C. L. Pueyo and M. Krumm, *Inorg. Chim. Acta*, 2010, **363**, 4148–4157.
41 S. Polarz, *Adv. Funct. Mater.*, 2011, **21**, 3214–3230.
42 S. Mann and G. A. Ozin, *Nature*, 1996, **382**, 313–318.
43 J. Park, J. Joo, S. G. Kwon, Y. Jang and T. Hyeon, *Angew. Chem., Int. Ed.*, 2007, **46**, 4630–4660.
44 A. Guinier, *X-ray Crystallographic Technology*, Hilger and Watts, London, 1952.
45 A. Guinier and G. Fournet, *Small-Angle Scattering of X-rays*, John Wiley, New York, 1955.
46 J. S. Reparaz, L. R. Muniz, M. R. Wagner, A. R. Goni, M. I. Alonso, A. Hoffmann and B. K. Meyer, *Appl. Phys. Lett.*, 2010, **96**, 231906.
47 S. Polarz, A. Orlov, A. Hoffmann, M. R. Wagner, C. Rauch, R. Kirste, W. Gehlhoff, Y. Aksu, M. Driess, M. W. E. van den Berg and M. Lehmann, *Chem. Mater.*, 2009, **21**, 3889–3897.
48 R. Kirste, Y. Aksu, M. R. Wagner, S. Khachadorian, S. Jana, M. Driess, C. Thomsen and A. Hoffmann, *ChemPhysChem*, 2011, **12**, 1189–1195.
49 H. K. Yadav, K. Sreenivas, V. Gupta and R. S. Katiyar, *J. Appl. Phys.*, 2008, **104**, 053507.
50 M. Schirra, R. Schneider, A. Reiser, G. M. Prinz, M. Feneberg, J. Biskupek, U. Kaiser, C. E. Krill, K. Thonke and R. Sauer, *Phys. Rev. B: Condens. Matter Mater. Phys.*, 2008, **77**, 125215.
51 M. R. Wagner, G. Callsen, J. S. Reparaz, J. H. Schulze, R. Kirste, M. Cobet, I. A. Ostapenko, S. Rodt, C. Nenstiel, M. Kaiser, A. Hoffmann, A. V. Rodina, M. R. Phillips, S. Lautenschlager, S. Eisermann and B. K. Meyer, *Phys. Rev. B: Condens. Matter Mater. Phys.*, 2011, **84**, 035313.
52 C. Rauch, W. Gehlhoff, M. R. Wagner, E. Malguth, G. Callsen, R. Kirste, B. Salameh, A. Hoffmann, S. Polarz, Y. Aksu and M. Driess, *J. Appl. Phys.*, 2010, **107**, 024311.
53 W. E. Carlos, E. R. Glaser and D. C. Look, *Phys. B*, 2001, **308**, 976–979.
54 M. Tiemann, *Chem.–Eur. J.*, 2007, **13**, 8376–8388.
55 S. Polarz, A. Roy, M. Lehmann, M. Driess, F. E. Kruis, A. Hoffmann and P. Zimmer, *Adv. Funct. Mater.*, 2007, **17**, 1385–1391.